Impact of Confinement on Zeolite Cracking Selectivity via Monte Carlo Integration

Michael D. Macedonia and Edward J. Maginn
Dept. of Chemical Engineering and The Center for Catalysis and Reaction Engineering, University of Notre Dame, Notre Dame, IN 46556

Monte Carlo integration methods employing a classic molecular mechanics force field were used to probe the impact of confinement on the selectivity of the n-hexane/3-methylpentane test reaction in 12 different zeolites. The simulations estimated relative cracking rates and predicted the constraint index (CI) selectivity for both monomolecular and bimolecular cracking mechanisms. By comparing with experimentally measured values of the CI, information on the dominant mechanism responsible for the observed selectivity was obtained. For small-pore zeolites, the monomolecular mechanism dominated, with the measured CI attributed to reactant selectivity based on preferential adsorption. For large-pore zeolites, the CI selectivity was attributed to confinement effects imposed on the bimolecular transition states. For zeolite structures with intermediate-sized pores, such as MTW and TON, the simulations indicated that both reaction mechanisms may be operative. The experimentally observed reduction in the CI with temperature in ZSM-5 can be explained in terms of the relative importance of steric and entropic factors in the stabilization of the bimolecular transition state. A change in mechanism from bimolecular to monomolecular, as postulated in the literature, is not necessary to explain the experimentally observed temperature dependence of the CI.

Introduction

Zeolites are crystalline microporous aluminosilicates that are used widely as absorbents and catalysts. The unique adsorption and catalytic properties of zeolites are due in large part to intimate interactions between guest molecules (reactants or sorbates) and the zeolite framework. Depending on the zeolite architecture, molecules of a certain size and shape may be excluded from entering the pores. This effect is known as *molecular sieving*. Zeolites often are used in *shape-selective* catalysis, which takes advantage of these molecular sieving properties.

Over the years, various "test reactions" have been developed as a means of quantifying the shape selectivity of zeolites and deducing the structure of new materials of unknown pore size. One of the first test reactions to be used is based upon the competitive cracking of *n*-hexane and 3-methylpentane. Selectivity is measured in terms of the disappearance of reactants via a "constraint index" (CI) (Frillette et al., 1981). A related test reaction that measures the appearance of products and yields a "refined" constraint index (CI*), is based on the ratio of 2-methylnonane and 5-methylnonane appearing in the product stream during the isomerization of *n*-decane (Martens et al., 1984). It is imperative in any test reaction that the difference in selectivity between zeolites be due to the pore architecture and not to other factors, such as the strength of active sites or the size of the zeolite crystals. As a result, no single test reaction is effective in characterizing the full range of zeolite pore sizes and types. A summary of many commonly used test reactions may be found in the review by Weitkamp and Ernst (1994).

While test reactions are useful in helping categorize zeolites according to pore size, it is difficult from these experiments to identify the actual mechanism responsible for the observed selectivity. Five main steps can be identified in a

Correspondence concerning this article should be addressed to E. J. Maginn.

cracking reaction where the architecture of a zeolite pore network leads to the enhanced selectivity of one species over another. Step 1 involves the adsorption of reactants from the gas phase into the pores of the zeolite crystal. Step 2 involves the diffusion of the adsorbed reactants to the active sites of the zeolite, where the reactions are presumed to take place. Reactants that do not adsorb or diffuse to the active sites will not react and should be detected in the reactor effluent. Selectivity which arises from Steps 1 or 2 is known as *reactant shape selectivity*. Step 3 involves the formation of the transition state and subsequent product formation at the active sites. A zeolite may be spacious enough to allow for reactant molecules to freely adsorb and diffuse, yet not spacious enough to allow for transition-state formation. Selectivity, which arises from Step 3, is called *restricted transition-state shape selectivity*. Once products have formed, they must diffuse away from the active site to the surface of the zeolite crystal (Step 4) and then desorb into the gas phase (Step 5). Products that cannot diffuse away from the active site and desorb are reacted further, and thus will not appear in the effluent stream. Selectivity that is derived from limitations based on Steps 4 and 5 is known as *product shape selectivity*. Any one or a combination of these factors can lead to the observed shape selectivity for a zeolite. Deconvoluting these factors from the results of a test reaction is difficult. For example, it was long assumed that the selectivity observed in the CI test reaction for ZSM-5 was due to the superior mobility of *n*-hexane over 3-methylpentane, and thus was a clear case of reactant shape selectivity. It was later proven by Haag et al. (1982) that the CI of ZSM-5 was not due to transport effects, but rather was the result of restricted transition-state shape selectivity.

There have been a few theoretical attempts performed to understand selectivity effects in zeolites. An early molecular graphics study by Martens and coworkers (1988) investigated the restricted transition-state shape selectivity effect for the disproportionation of *m*-xylene in several zeolites. It was found that isomers whose formation depended on favorable fitting transition-state structures were the primary components of the experimental product distribution. Santilli et al. (1993) conducted a computational study that illustrated a link between the preferential adsorption of branched hydrocarbons and their formation during the hydrocracking of hexadecane. This study, based on "docking energy" calculations, concluded that product shape-selectivity effects were most apparent in 10-ring zeolites and less prevalent in 12-ring systems (*x*-ring means that the pores of zeolite are formed by rings containing *x* oxygen atoms; in zeolites, *x* is commonly 8, 10, or 12). A more recent computational study of product shape selectivity was performed by Webb and Grest (1998). Diffusion coefficients of various decane isomers were computed by molecular dynamics and then used to obtain estimates of CI*. It was found that the estimated values of CI* matched experimental trends for many zeolites, indicating that product shape selectivity plays some role in determining the product distribution in *n*-decane isomerization. Computed CI* values for zeolite structures such as EUO and FER, however, did not match the experimental trends. This indicates that other undetermined factors dictate the selectivity in these zeolites. There also has been a large number of quantum chemical calculations performed on zeolite catalysts (Boronat et al., 1998; van Santen, 1997). Nicholas (1997) has reviewed much of this literature. Although these studies have provided a great deal of information about the nature of the active sites in zeolites and the transition states, most of these calculations have relied on the use of molecular clusters to represent active sites in a zeolite. Thus, these methods cannot be used to assess the impact of diffusion, adsorption, and confinement on selectivity.

The goal of the present study is to examine the role pore structure plays on the CI. Using a detailed atomistic representation of the reactant species and transition-state complexes within 12 distinct zeolite structures, Monte Carlo integration methods will be used to estimate relative constraint indices for the different zeolites. Comparison with experimentally measured CIs will be made in an attempt to understand the selectivity trends observed in the simulations and pinpoint the sources of selectivity for the various zeolite structures. In particular, we will assess when adsorption and confinement are important factors in the experimentally measured CI. Such a study is important for several reasons. First, it has been demonstrated experimentally that adsorption, diffusion and confinement can impact cracking rates and product distributions (Williams et al., 1999). Second, standard quantum techniques are incapable of addressing these effects due to limitations that require the use of cluster models. Finally, it has been shown that the CI test can be an unreliable predictor for the structure of a zeolite, especially when one considers new zeolite structure types (Zones and Harris, 2000). Thus it would be useful if theory could provide guidance to help interpret the CI test reaction results and make predictions as to when adsorption and confinement effects should be important. We emphasize that the goal of the current work is not to model all the reaction pathways present in hydrocarbon cracking. Rather, our more modest goal is to develop a framework in which relatively simple classic molecular modeling methods can be used to assess the impact of pore structure on selectivity in the standard CI test reaction.

Theory

Mechanisms of cracking on zeolites

Catalytic cracking has been the subject of intense study for many years. Although there are still unanswered questions regarding the details, there are two generally accepted mechanisms for paraffin cracking in zeolites (Haag and Dessau, 1984; Pines, 1981). The first mechanism, known variously as *monomolecular* or *protolytic* cracking, involves the direct protonation of an alkane by an acid site to form a high-energy pentacoordinated carbonium ion:

$$CR_2H_2 + H^+ \rightarrow [CR_2H_3]^+. \qquad (1)$$

This carbonium ion can then collapse to form either molecular hydrogen and an adsorbed carbenium ion

$$[CR_2H_3]^+ \rightarrow [CR_2H]^+ + H_2, \qquad (2)$$

or a smaller alkane and a different carbenium ion

$$[CR_2H_3]^+ \rightarrow RH + [CRH_2]^+. \quad (3)$$

The acid site is regenerated when the carbenium ion desorbs to form an alkene. Alternatively, the carbenium ions may serve as active sites themselves in a bimolecular mechanism (described below). *Ab initio* calculations performed by Kazansky et al. (1994, 1996) and Kazansky (1999) have suggested that the pentacoordinated carbonium-ion transition-states exist as highly excited short-lived species tightly bound to the active sites of the zeolite.

A second mechanism of paraffin cracking, known as the *bimolecular* mechanism, occurs via a chain reaction involving carbenium ions (Pines, 1981; Haag et al., 1991). The first step in the reaction involves a hydride transfer between the feed paraffin and a smaller adsorbed carbenium ion (Williams et al., 1999).

$$R_iH + [R_j]^+ \rightarrow [R_i]^+ + R_jH \qquad (j < i). \quad (4)$$

Following this initiation step, the adsorbed carbenium ion cracks by β-scission (cleavage of the C–C bond located β to the trivalent positively charged carbon atom) to form an alkene and a new adsorbed carbenium ion that propagates the reaction:

$$[R_i]^+ \rightarrow \text{alkene} + [R_j]^+. \quad (5)$$

Isomerization of the carbenium ion may take place between these steps. The initial carbenium ion in Eq. 4 can arise from protonation of olefinic feed impurities or direct protonation of the paraffin feed molecules via the monomolecular mechanism (Haag and Dessau, 1984). The reaction illustrated in Eq. 5 occurs rapidly, and thus the hydride transfer of Eq. 4 is the rate-determining step.

It has been found that the bimolecular mechanism predominates at lower temperatures, higher feed partial pressures, and higher conversions. The monomolecular mechanism has been found, conversely, to predominate at higher temperatures, lower feed partial pressures, and lower conversions. It was noted by Haag and Dessau (1984) that the structure of the zeolite catalyst also plays a major role in determining which mechanism dominates. The bimolecular mechanism seems to be more important in larger pore zeolites, while the monomolecular mechanism is more important in smaller pore zeolites. Presumably this is due to the lack of space available in small pore zeolites for formation of the bimolecular complexes that must be formed in Eq. 4.

Constraint index test reaction

The CI experiment is performed by passing a stream containing equal mole fractions (0.1 at 1 atm) of *n*-hexane (*nC6*) and 3-methylpentane (*3mC5*) over the zeolite catalyst at a temperature that yields conversions of approximately 10% (Frillette et al., 1981). The experimentally measured quantity is computed by

$$CI = \frac{\log(1 - X_{nC6})}{\log(1 - X_{3mC5})} \quad (6)$$

where X is the conversion of the species. Assuming first-order kinetics, this is equivalent to the ratio of the reaction rates for the reactant species (Weitkamp and Ernst, 1994)

$$CI \equiv \frac{r^{nC6}}{r^{3mC5}} = \frac{k^{nC6}[nC6]}{k^{3mC5}[3mC5]} = \frac{k^{nC6}}{k^{3mC5}}, \quad (7)$$

where k is an apparent first-order reaction rate constant, while $[nC6]$ and $[3mC5]$ are the inlet gas-phase concentrations, which are equal in this experiment. The CI measurements have been used to classify zeolites into three major groups. CI values of less than 1 indicate large-pore (12-ring) zeolites; values of between 1 and 10 indicate medium-pore (10-ring) zeolites; and values greater than 10 indicate small-pore (8-ring) crystals.

The variation of CI with pore size is due, in some capacity, to the confinement and transport effects imposed on the reactants and transition states by the zeolite framework. It is widely known that, on acidic catalysts, branched alkanes are cracked at a faster rate than *n*-alkanes (Weitkamp and Ernst, 1994). Thus, it is not surprising that this is the case for large-pore zeolites, where confinement effects are not important and *3mC5* is cracked at a higher rate than *nC6*. This results in values of the CI that are less than 1. For the 10-ring zeolites, confinement effects become more important, as the cracking of branched isomers is hindered with respect to that of straight-chain isomers. The resulting CI values are greater than 1, indicating enhanced selectivity for the cracking of *n*-hexane. In small-pore (8-ring) zeolites, the cracking of $3mC_5$ is strongly hindered, resulting in very high values of the CI.

The temperature dependence of the CI is troublesome in that it adds another variable to the reaction selectivity. Increasing the temperature of the reaction generally results in a decrease in the selectivity of the reaction. For example, Frillette et al. (1981) found that the CI of ZSM-5 was reduced from 11 to 1 by increasing the temperature of the reaction by 220 K. The temperature dependence of the CI has been rationalized in part by assuming a bimolecular cracking mechanism at lower temperatures and a monomolecular cracking mechanism at high temperatures (Haag et al., 1982, 1984). Presumably, the selectivity of these two reaction mechanisms is impacted by pore size.

Model reaction network for CI

Although the CI provides an experimental means for characterizing a catalyst, it yields little insight into which of the competing mechanisms are responsible for the observed selectivity. Furthermore, the rate expressions in Eq. 7 are based on gas-phase reactant concentrations, which may not reflect the actual composition at the active sites. To shed light on the sources of cracking selectivity, a reaction network based on the five fundamental reaction steps (adsorption, diffusion to an active site, transition-state formation, diffusion away from the active site, and desorption) is developed below. The formulation is general for two reactants A and B. For the CI reactions, A represents *n*-hexane and B represents 3-methylpentane.

Step 1: Adsorption of Reactants. The adsorbed reactants are assumed to be in equilibrium with the gas phase, so that

$$A \overset{K^A}{\longleftrightarrow} A^* \tag{8}$$

$$B \overset{K^B}{\longleftrightarrow} B^*, \tag{9}$$

where the species on the left side of the equations are in the gas phase, $(*)$ denotes a species adsorbed in the zeolite, and K^A and K^B are equilibrium constants for the adsorption process, given by

$$K^A = \frac{[A^*]}{[A]} \tag{10}$$

$$K^B = \frac{[B^*]}{[B]}. \tag{11}$$

The zeolite active sites are assumed to be located uniformly throughout the pores, so that $[A^*]$ and $[B^*]$ represent the reactant concentrations at the zeolite active sites. This is clearly an oversimplification, but lacking information on the exact location of active sites, it is a necessary approximation.

Step 2: Diffusion of Reactants. Diffusion of the reactants is assumed to be fast, such that transport to the active sites is not rate limiting. This assumption is valid for many zeolites at the high reaction temperatures used to evaluate the CI. It will not be valid for all systems, however, so that the present analysis is expected to break down for diffusion-limited systems. Discrepancies with experiment can be used to identify possible cases of diffusion limitation, as discussed more fully in the Results and Discussion section.

Step 3: Formation of Transition-States. The monomolecular transition-state formation mechanisms can be written as

$$A^* + \mathrm{H}^+ \xrightarrow{k_m^A} [A - \mathrm{H}^+]^{\ddagger} \tag{12}$$

$$B^* + \mathrm{H}^+ \xrightarrow{k_m^B} [B - \mathrm{H}^+]^{\ddagger}, \tag{13}$$

where k_m^A and k_m^B are second-order reaction-rate constants, H^+ represents a zeolite acid site, and $(\ddagger)$ represents an activated transition-state complex. The decomposition of the activated complexes is fast, and thus not rate limiting. For the bimolecular mechanism, we will assume that the adsorbed carbenium ion is a bound propyl carbocation. The bimolecular transition-state formation reaction can thus be written as

$$A^* + \mathrm{C}_3^+ \xrightarrow{k_b^A} [A - \mathrm{C}_3^+]^{\ddagger} \tag{14}$$

$$B^* + \mathrm{C}_3^+ \xrightarrow{k_b^B} [B - \mathrm{C}_3^+]^{\ddagger}, \tag{15}$$

where k_b^A and k_b^B represent the second-order rate constants for the bimolecular mechanism, and C_3^+ is the propyl carbenium ion. As in the monomolecular case, the subsequent decomposition of the transition states is assumed to be fast. Note that the rate-limiting steps are written as second-order reactions involving the concentration of adsorbed paraffin reactants and either the concentration of acidic protons (monomolecular) or carbenium ions (bimolecular). This formulation explicitly accounts for the fact that the concentration of these active sites can depend on the material and operating conditions, and that the concentration of reactants at the active sites can be very different from the gas-phase composition. This is in contrast to the usual way the CI is defined as a first-order reaction using the gas-phase concentration of the reactants (see Eq. 7). We believe the mechanisms given here are more faithful to the actual reaction process and will enable different selectivity effects to be isolated.

Step 4: Diffusion of Products. In accordance with the assumption that reactant diffusion is not limiting, the cracked products are assumed to be highly mobile, so that this step is not limiting. This assumption is likely to be a good one, since the cracked products are smaller than the reactants.

Step 5: Desorption of Products. The product concentrations in the gas phase are dilute, so that at equilibrium the concentrations of products in the zeolite will also be small. Thus desorption should be facile, and is assumed to have no impact on selectivity.

Statistical mechanical formulation of the CI

Given the fundamental steps and assumptions made in the previous section, a statistical mechanical formulation for computing the CI from a molecular model can now be developed. If formation of the transition state is the rate-limiting step in the cracking process, then the overall rate expressions are given by

$$r_m^A = k_m^A [A^*][\mathrm{H}^+] \tag{16}$$

$$r_m^B = k_m^B [B^*][\mathrm{H}^+] \tag{17}$$

$$r_b^A = k_b^A [A^*][\mathrm{C}_3^+] \tag{18}$$

$$r_b^B = k_b^B [B^*][\mathrm{C}_3^+], \tag{19}$$

where the subscripts m and b designate monomolecular and bimolecular reactions, respectively. Assuming that both species are cracked via the monomolecular mechanism, Eqs. 16 and 17 are substituted into Eq. 7 to yield a monomolecular constraint index:

$$CI_m = \frac{r_m^A}{r_m^B} = \frac{k_m^A}{k_m^B} \frac{[A^*]}{[B^*]}, \tag{20}$$

where the concentration of the zeolite acid sites has canceled. If both species are cracked by the bimolecular mechanism, an expression for the bimolecular constraint index is obtained through substitution of Eqs. 18 and 19 into Eq. 7:

$$CI_b = \frac{r_b^A}{r_b^B} = \frac{k_b^A}{k_b^B} \frac{[A^*]}{[B^*]}, \tag{21}$$

where it is assumed that the concentration of the propyl carbenium ions are equal in both reactions. Replacing the reactant concentrations in Eqs. 20 and 21 with Eqs. 10 and 11, and noting that the gas-phase compositions are equal in the

CI experiment ($[A]=[B]$) gives

$$CI_m = \frac{k_m^A}{k_m^B}\frac{K^A}{K^B} \tag{22}$$

$$CI_b = \frac{k_b^A}{k_b^B}\frac{K^A}{K^B}. \tag{23}$$

It is then postulated that the intrinsic rate constants that appear in Eqs. 16–19 are the product of two factors. The first factor describes the inherent rate with which the reactant is activated by an acid site, and the second factor accounts for the impact molecular confinement has on the ability to form the transition state. These two factors can be represented by *electronic* and *confinement* rate constants in the following manner

$$k_m^A = k_{m,e}^A\, k_{m,c}^A \tag{24}$$

$$k_m^B = k_{m,e}^B\, k_{m,c}^B \tag{25}$$

$$k_b^A = k_{b,e}^A\, k_{b,c}^A \tag{26}$$

$$k_b^B = k_{b,e}^B\, k_{b,c}^B. \tag{27}$$

It is known that the cracking reactivity of a branched species is greater than that of a comparable linear species when there are no confinement effects. This difference in reactivity can be attributed to a higher *electronic* rate constant for the branched species. On the other hand, different zeolites can exhibit vastly difference selectivities for linear over branched species, even though quantum calculations (Sauer, 1994) and experiments (Babitz et al., 1999) have shown that the nature of the acid sites does not vary that much between different zeolites. These large rate variations must be due to adsorption and confinement effects brought about by the differences in pore topography. These effects will be captured in the *confinement* rate constant.

In principle, both the electronic and confinement terms in Eqs. 24–27 could be evaluated in a quantum mechanical calculation. At the present time, however, limitations on the number of atoms that can be simulated using high-level methods prohibit the calculation of confinement effects for almost all zeolites. Classic simulation methods within a transition-state theory framework will thus be used to estimate the relative importance of confinement on the CI. Since the nature of active sites is similar across different zeolites, the electronic rate constants are assumed to be only a function of the reaction mechanism, *and not the specific zeolite*. Although this is clearly an oversimplification, it allows classic simulations to be used to assess the relative importance of confinement on selectivity, enabling a direct comparison to be made between computed and experimental values of the CI with limited computational expense.

Within a transition-state theory formalism, the confinement rate constant for a given species is proportional to the ratio of transition state and reactant partition functions (Laidler, 1969). For the case of a zeolite, the confinement rate constant for the monomolecular reaction of A is given by (June et al., 1990)

$$k_{m,c}^A = S_1 \frac{\int_{(A-H^+)^\ddagger} \exp\left[\frac{-\nabla\left(q^{(A-H^+)^\ddagger}\right)}{k_B T}\right] dq^{(A-H^+)^\ddagger}}{\int_A \exp\left[\frac{-\nabla\left(q^A\right)}{k_B T}\right] dq^A \int_{H^+} \exp\left[\frac{-\nabla\left(q^{H^+}\right)}{k_B T}\right] dq^{H^+}}, \tag{28}$$

where S_1 is a constant specific to this reaction, ∇ is the potential energy that can be computed from a molecular model, k_B is the Boltzmann constant, T is the temperature, and $\boldsymbol{q}$ is the vector of generalized coordinates that describes the positions of the reactant and transition-state species. A similar expression for $k_{m,c}^B$ can be written with a different constant, S_2. The integral in the numerator of Eq. 28 is over the transition-state complex, which is localized at a dividing surface separating reactants from products. Details on how the transition-state structures are determined will be given later. The integrals in the denominator are over the reactant molecule A and the proton. Note that the reactants have one more degree of freedom than the transition state. By virtue of the assumption of uniformly dispersed active sites, and because the concentration of reactants is low under reaction conditions, the integrals in Eq. 28 are carried out independently for a single molecule of each species over the entire zeolite pore volume. If the location of the active site is known, the integration volume in Eq. 28 may be limited to those regions.

For the bimolecular mechanism, the confinement rate constant for the reaction of A is given by

$$k_{b,c}^A = S_3 \frac{\int_{(A-C_3^+)^\ddagger} \exp\left[\frac{-\nabla\left(q^{(A-C_3^+)^\ddagger}\right)}{k_B T}\right] dq^{(A-C_3^+)^\ddagger}}{\int_A \exp\left[\frac{-\nabla\left(q^A\right)}{k_B T}\right] dq^A \int_{C_3^+} \exp\left[\frac{-\nabla\left(q^{C_3^+}\right)}{k_B T}\right] dq^{C_3^+}}, \tag{29}$$

where the terms have the similar meaning to those in Eq. 28. A similar expression can be obtained for $k_{b,c}^B$ using a different constant S_4. These rate constants can be written in shorthand notation:

$$k_{m,c}^A = S_1 \frac{Z_a^{(A-H^+)^\ddagger}}{Z_a^A Z_a^{H^+}} \tag{30}$$

$$k_{m,c}^B = S_2 \frac{Z_a^{(B-H^+)^\ddagger}}{Z_a^B Z_a^{H^+}} \tag{31}$$

$$k_{b,c}^A = S_3 \frac{Z_a^{(A-C_3^+)^\ddagger}}{Z_a^A Z_a^{C_3^+}} \tag{32}$$

$$k_{b,c}^B = S_4 \frac{Z_a^{(B-C_3^+)^\ddagger}}{Z_a^B Z_a^{C_3^+}}, \tag{33}$$

where Z is a configurational integral, the superscript refers to the species, and the subscript (a) reminds us that these species are in the adsorbed phase. Substituting Eqs. 24–27 and Eqs. 30–33 into Eqs. 22 and 23 gives for the CIs

$$CI_m = \left(\frac{k^A_{m,e}}{k^B_{m,e}}\right)\left(\frac{S_1 Z_a^{(A-H^+)^\ddagger} Z_a^B Z_a^{H^+}}{S_2 Z_a^{(B-H^+)^\ddagger} Z_a^A Z_a^{H^+}}\right)\left(\frac{K^A}{K^B}\right) \quad (34)$$

$$CI_b = \left(\frac{k^A_{b,e}}{k^B_{b,e}}\right)\left(\frac{S_3 Z_a^{(A-C_3^+)^\ddagger} Z_a^B Z_a^{C_3^+}}{S_4 Z_a^{(B-C_3^+)^\ddagger} Z_a^A Z_a^{C_3^+}}\right)\left(\frac{K^A}{K^B}\right). \quad (35)$$

The three terms in Eqs. 34 and 35 clearly demonstrate the fact that, for systems that are not diffusion limited, selectivity can arise from electronic, confinement, and/or adsorption effects. This result is in line with previous findings that the intrinsic activation energy for reactions is frequently related to the Henry's law constant or the heat of adsorption (Haag et al., 1981; van de Runstraat et al., 1997; Derouane, 1998; Maeson et al., 1999).

The partitioning coefficients for adsorption can be expressed in terms of a ratio of configurational integrals (Maginn et al., 1995):

$$K^A = \left(\frac{Z_a^A}{Z_g^A}\right) \quad (36)$$

$$K^B = \left(\frac{Z_a^B}{Z_g^B}\right), \quad (37)$$

where Z_g^A and Z_g^B are *gas-phase* configurational integrals. Assuming that the gas phase is ideal, Z_g^A and Z_a^B are evaluated by integrating over the intramolecular portion of the potential energy for single molecules of A and B. Substituting Eqs. 36 and 37 into Eqs. 34 and 35 and canceling terms yields:

$$CI_m = \left(\frac{k^A_{m,e}}{k^B_{m,e}}\right)\left(\frac{S_1 Z_a^{(A-H^+)^\ddagger} Z_g^B}{S_2 Z_a^{(B-H^+)^\ddagger} Z_g^A}\right) \quad (38)$$

$$CI_b = \left(\frac{k^A_{b,e}}{k^B_{b,e}}\right)\left(\frac{S_3 Z_a^{(A-C_3^+)^\ddagger} Z_g^B}{S_4 Z_a^{(B-C_3^+)^\ddagger} Z_g^A}\right). \quad (39)$$

The computed constraint indices in Eqs. 38 and 39 are composed of the product of an *electronic* and a *confinement* term. Treatment of the electronic term will be explained later. The confinement terms will be evaluated via Monte Carlo integration. Given that a classic force field with no electrostatics is used (see below for explanation), it is safe to assume that the transition-state complexes for the monomolecular mechanism are sufficiently identical to the adsorbed feed molecules such that

$$\frac{Z_a^{(A-H^+)^\ddagger}}{Z_a^{(B-H^+)^\ddagger}} \approx \frac{Z_a^A}{Z_a^B}. \quad (40)$$

Substitution of this expression into Eq. 38 yields the final form of CI_m:

$$CI_m = \left(\frac{k^A_{m,e}}{k^B_{m,e}}\right)\left(\frac{S_1 Z_a^A Z_g^B}{S_2 Z_a^B Z_g^A}\right). \quad (41)$$

To evaluate CI_m, Monte Carlo integration of single $nC6$ (A) and $3mC5$ (B) molecules is performed in the gas and adsorbed phase.

The transition-states for the bimolecular reaction are much different from the feed molecules (see Figure 1), so that Eq. 39 is the final form for CI_b. Gas-phase Monte Carlo integration of $nC6$ (A) and $3mC5$ (B) as well as adsorbed phase simulations of $nC6_b^{TS}$ $[(A-C_3^+)^\ddagger]$ and $3mC5_b^{TS}[(B-C_3^+)^\ddagger]$ are necessary to evaluate CI_b.

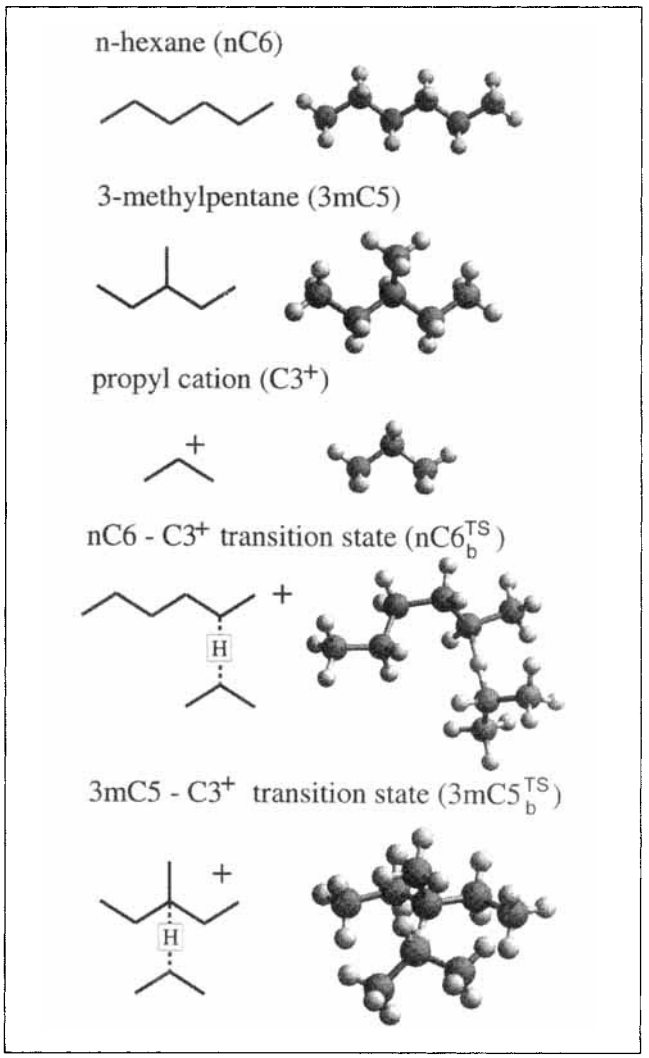

Figure 1. Molecules simulated in this work.

n-Hexane and 3-methylpentane molecules must be simulated for both the monomolecular and bimolecular mechanisms. The propyl cation and bimolecular transition states need only be simulated for the bimolecular mechanism.

Normalized CI for comparison with experiment

The electronic contribution of the CI cannot be computed using classic simulation techniques. In addition, the constants S_1, S_2, S_3, and S_4 are difficult to evaluate for complex molecules (June et al., 1990). These issues make a direct comparison between computed values of CI_m and CI_b and experimental values of CI impossible. To circumvent this problem, the computed and experimental CI values for each zeolite (i) will be normalized by the CI for a reference zeolite (REF). The computed, normalized monomolecular constraint index is given by

$$\overline{CI}_m^{\mathrm{REF}} \equiv \frac{CI_m(i)}{CI_m(\mathrm{REF})} = \frac{\left(\frac{k_{m,e}^A(i)}{k_{m,e}^B(i)}\right)\left(\frac{S_1 Z_a^A(i) Z_g^B(i)}{S_2 Z_a^B(i) Z_g^A(i)}\right)}{\left(\frac{k_{m,e}^A(\mathrm{REF})}{k_{m,e}^B(\mathrm{REF})}\right)\left(\frac{S_1 Z_a^A(\mathrm{REF}) Z_g^B(\mathrm{REF})}{S_2 Z_a^B(\mathrm{REF}) Z_g^A(\mathrm{REF})}\right)}, \quad (42)$$

where (i) indicates a quantity computed in zeolite i (and at temperature T_i), and (REF) indicates a quantity computed in the reference zeolite at temperature T_{REF}. If the electronic rate constants are only functions of the reaction mechanism and are independent of the zeolite, they may be eliminated if a reference zeolite is chosen that exhibits cracking based only on the appropriate mechanism. For example, if one wishes to evaluate $\overline{CI}_m^{\mathrm{REF}}$, one must choose a reference zeolite in which the feed paraffins are cracked primarily by the monomolecular mechanism. Selection of an appropriate reference zeolite leads to a cancellation of terms, yielding

$$\overline{CI}_m^{\mathrm{REF}} = \left(\frac{Z_a^A(i) Z_g^B(i)}{Z_a^B(i) Z_g^A(i)}\right)\left(\frac{Z_a^B(\mathrm{REF}) Z_g^A(\mathrm{REF})}{Z_a^A(\mathrm{REF}) Z_g^B(\mathrm{REF})}\right), \quad (43)$$

where the gas-phase integrals cancel only if $T_i = T_{\mathrm{REF}}$, and the constants (S_1 and S_2) will cancel regardless of the temperatures. As a first-order approximation, the ratio of electronic terms in Eq. 42 is assumed to be a weak function of temperature relative to the confinement terms, and so this ratio does not appear in Eq. 43. The computed $\overline{CI}_m^{\mathrm{REF}}$ is then compared with an experimental reference CI, given by

$$\overline{CI}^{REF} = \frac{CI(i)}{CI(\mathrm{REF})}, \quad (44)$$

where $CI(i)$ and CI(REF) are experimentally measured.

The computed bimolecular reference CI is given by the ratio of values computed using Eq. 39

$$\overline{CI}_b^{\mathrm{REF}} \equiv \frac{CI_b(i)}{CI_b(\mathrm{REF})} = \frac{\left(\frac{k_{b,e}^A(i)}{k_{b,e}^B(i)}\right)\left(\frac{S_3 Z_a^{(A-C_3^+)^\ddagger}(i)\, Z_g^B(i)}{S_4 Z_a^{(B-C_3^+)^\ddagger}(i) Z_g^A(i)}\right)}{\left(\frac{k_{b,e}^A(\mathrm{REF})}{k_{b,e}^B(\mathrm{REF})}\right)\left(\frac{S_3 Z_a^{(A-C_3^+)^\ddagger}(\mathrm{REF}) Z_g^B(\mathrm{REF})}{S_4 Z_a^{(B-C_3^+)^\ddagger}(\mathrm{REF}) Z_g^A(\mathrm{REF})}\right)}, \quad (45)$$

where the appropriate reference zeolite is now one in which the feed paraffins are cracked mainly by the bimolecular mechanism. Note that the reference zeolite for the $\overline{CI}_b^{\mathrm{REF}}$ *must* be different from the one used for $\overline{CI}_m^{\mathrm{REF}}$. Cancellation of terms in Eq. 45 after selection of an appropriate reference zeolite yields

$$\overline{CI}_b^{\mathrm{REF}} = \left(\frac{Z_a^{(A-C_3^+)^\ddagger}(i) Z_g^B(i)}{Z_a^{(B-C_3^+)^\ddagger} Z_g^A(i)}\right)\left(\frac{Z_a^{(B-C_3^+)^\ddagger}(\mathrm{REF}) Z_g^A(\mathrm{REF})}{Z_a^{(A-C_3^+)^\ddagger}(\mathrm{REF}) Z_g^B(\mathrm{REF})}\right), \quad (46)$$

which would then be compared to Eq. 44 using the same reference zeolite. Selection of the reference zeolites for the monomolecular and bimolecular mechanisms are discussed in the Results and Discussion section.

Model and Simulation Details

Force field and transition-state structure

A fully atomistic representation of the reactants, products, and zeolite are used for all calculations. The molecular mechanics force field used in this work is based primarily on the consistent valence force field (CVFF) (Hagler et al., 1979). The interactions between atoms of adsorbate molecules and atoms of the zeolite are modeled by a 12-6 Lennard-Jones potential. Bond lengths are fixed, bond angles are modeled using a harmonic potential function, and dihedral angles are treated using an appropriately parameterized cosine expansion. All the parameters used in the current work are given in Table 1. Additional details concerning the form of the force field may be found elsewhere (Macedonia and Maginn, 1999).

The bimolecular transition states consist of a carbenium ion, represented by an adsorbed propyl carbocation, and an adsorbed paraffin. A hydrogen atom is transferred between the paraffin and carbenium ion. Structures for the bimolecular transition states were determined from semiempirical

Table 1. Force Field Parameters Used in This Work

Nonbond	A [kJ·Å^{12}·mol^{-1}]	B [kJ·Å^{6}·mol^{-1}]
C	7,490,785.5892	2,211.1683
H	29,741.8217	137.531
H^{TS}	29,741.8217	137.531
O	1,141,791.7788	2,087.3089
Si	0	0
Bond Angle	k_θ [kJ·rad^{-2}·mol^{-1}]	θ_0 [deg]
C–C–C	194.974	110.50
H–C–H	165.268	106.40
C–C–H	185.770	110.00
C–H^{TS}–C	19.497	175.00
Torsion	k_ϕ [kJ·mol^{-1}]	$n - \phi_0$ [deg]
–C–C–	5.9517	3–0
–C–H^{TS}–	0	3–0

Note: Geometric combining rules are applied to nonbond parameters: $A_{ij} = \sqrt{A_i A_j}$ and $B_{ij} = \sqrt{B_i B_j}$. A (*) denotes that an atom of any identity can occupy the end positions in a dihedral angle.

quantum calculations using MOPAC6 with the MNDO approximation (Dewar and Theil, 1977). The optimization to the transition-state was done in the gas phase. It was assumed that these structures give a reasonable description of the shape of the transition-states in each of the different zeolites. A more sophisticated approach would be to optimize a different transition-state within each zeolite using higher level quantum calculations. As was pointed out earlier, however, computational limitations as well as uncertainty regarding the location of active sites in the zeolites prohibits this. The transferred hydrogen (H^{TS}) was located midway between the paraffin and propyl group carbon atoms, with a fixed $C-H^{TS}$ bond length of 1.359 Å. The $C-H^{TS}-C$ bond angle was found to be 175 degrees. To facilitate subsequent calculations, a weak force constant for this bond angle was developed to match the angle distribution that arose from an independent Metropolis Monte Carlo simulation of the transition-state molecule. This force constant was then used in the biasing algorithm for generating transition-state conformations. The efficiency of the simulations was increased by avoiding conformations of the transition-state in which there is significant steric overlap (Macedonia and Maginn, 1999). The torsional force constant was set to 0 for angles that rotate about the $C-H^{TS}$ bonds so that the transition-states would have maximum flexibility.

Electrostatic interactions were neglected in these calculations for two reasons. First, this study mainly concerns steric confinement effects, which are adequately treated using a 12-6 potential. The fact that ratios of configurational integrals of similarly charged species are computed serves to moderate the impact of charges on the current results. The second reason for neglecting electrostatics is that there is uncertainty regarding the location and chemical nature of acid sites in many of the zeolites under study. Including protons in these systems would necessarily involve some arbitrary guesswork, which could cloud some of the issues being investigated. Obviously, the use of a more detailed model would be preferred, but in this first attempt it was deemed sufficient to focus on systems without electrostatics.

Additional details

The simulations of reactant and transition-state molecules were carried out using the configurational-bias Monte Carlo integration (CB-MCI) technique for all-atom models. Complete details on the calculation of Z can be found in a previous work (Macedonia and Maginn, 1999). The zeolite lattice was assumed to be fixed in space for the duration of the simulations. Prior to the start of a simulation, 12-6 interactions between adsorbate atoms and atoms in the zeolite lattice were tabulated on a three-dimensional (3-D) grid for later interpolation (June et al., 1990). The 3-D grid used in this work was improved from the original formulation to allow the simulation of nonorthorhombic systems.

The size of the simulation box ranged from $2\times2\times2$ zeolite unit cells (for large unit-cell systems like FAU and BEA) to $3\times3\times7$ unit cells (for small unit-cell systems like TON). In each case, the box was large enough so that the minimum image convention was obeyed with a cutoff of 13.8 Å. An MC integration step consists of constructing the molecule from scratch using configurational-bias techniques and then computing its potential energy. The configurational integral is then updated with each progressive step until the value of the integral has converged. The reactant molecules (e.g., *nC6*, *3mC5*, and $C3^+$) converged within 1 million integration steps, while the transition-state molecules took on the order of 10 million steps to converge. These calculations were performed on a cluster of Sun ULTRA-Sparc workstations at the University of Notre Dame. Simulations took less than 10 h each for the reactant molecules and up to 3 days for the transition state. The longer convergence times for the transition-state results from the difficulty of finding low-energy conformations of these very bulky (see Figure 1) molecules in the confined pores of zeolites. The use of biasing methods is essential to the calculation of configurational integrals for these molecules. Such calculations are intractable by standard MC methods.

Results and Discussion

To gauge the confinement effects on the CI reaction, 12 different zeolite structures representing several types of cages and pores were investigated. Structural details regarding each of the zeolites are summarized in Table 2. All zeolite structures used in the calculations were taken from the library of structures included in Cerius[2] from Molecular Simulations Inc. (MSI), San Diego, CA USA.

The analysis of a constraint index based on a bimolecular reaction mechanism CI_b may not be appropriate for some small-pore zeolites. Therefore, zeolites in which the formation of a bimolecular transition state is prevented by confinement effects must first be identified. To do this, the quantities γ^A and γ^B are defined, which relate the bimolecular formation rates of a species (A or B) in a given zeolite to the formation rate in a reference zeolite that exhibits minimal confinement effects. Quantity γ^A is defined as

$$\gamma^A \equiv \frac{k^A_{b,c}(i)[A^*]^{(i)}[C_3^+]^{(i)}}{k^A_{b,c}(\mathrm{REF})[A^*]^{(\mathrm{REF})}[C_3^+]^{(\mathrm{REF})}}, \tag{47}$$

where quantities denoted by (i) are evaluated in zeolite i at temperature T_i, and quantities denoted by (REF) are evaluated in the reference zeolite at temperature T_{REF}. Substitution of Eq. 32 for the confinement rate constants, Eq. 36 for $[A^*]$, and canceling terms gives

$$\gamma^A = \left(\frac{Z_a^{(A-C_3^+)^\ddagger}(i)}{Z_a^{C_3^+}(i)Z_g^A(i)}\right)\left(\frac{Z_a^{C_3^+}(\mathrm{REF})Z_g^A(\mathrm{REF})}{Z_a^{(A-C_3^+)^\ddagger}(\mathrm{REF})}\right), \tag{48}$$

where it has been assumed that the concentrations of carbenium ions will not dominate the behavior of γ^A and thus cancel. An analogous expression can be written for γ^B. Notice that the calculation of $Z_a^{C_3^+}$ is necessary to evaluate γ^A and γ^B. The structure of C_3^+ is shown in Figure 1. The zeolite chosen as the reference zeolite is FAU, which comprises a spacious network of cages (see Table 2). For zeolites in which there are minimal confinement effects for bimolecular

Table 2. Zeolite Structural Information

IZA Code (Name) UC Dimensions	Pore Information	Comment
FAU (*X*,*Y*) Orthorhombic 25.0×25.0×25.0	Cages 7.4×7.4 Å (12-ring)	Small sodalite cages from a spacious network of supercages.
MOR (mordenite) Orthorhombic 18.1×20.5×7.5	[001] 6.5×7.0 Å (12-ring) [010] 2.6×5.7 Å (8-ring)	12-ring channel is flanked by 8-ring side pockets. For the purposes of this study, MOR is a 1-D system.
BEA (beta) Orthorhombic 12.7×12.7×26.4	[001] 7.6×6.4 Å (12-ring) [100] 5.5×5.5 Å (12-ring)	Spacious network of intersecting 12-ring channels.
MWW (MCM-22) Hexagonal 14.1×14.1×24.9	Supercages (12-ring) 7.1×7.1 Å ⊥ [001] sinusoidal (10-ring)	Two independent pore systems. Supercage network and sinusoidal 10-ring channels.
EUO (ZSM-50) Orthorhombic 13.7×22.3×20.2	[100] 4.1×5.7 Å (10-ring)	1-D with very spacious side pockets bordering the 10-ring channel.
MTW (ZSM-12) Monoclinic 24.9×5.0×24.3	[010] 5.5×5.9 Å (12-ring)	1-D puckered 12-ring system. Dimensions are really more like a typical 10-ring zeolite.
OFF (offretite) Hexagonal 13.3×13.3×7.6	[001] 6.7×6.7 Å (12-ring) ⊥ [001] 3.6×4.9 Å (8-ring)	Parallel [001] stacks of gmelinite cages (12-ring) and cancrinite cages (8-ring). This is a 2-D system.
FER (ZSM-35) Orthorhombic 19.2×14.1×7.5	[001] 4.2×5.4 Å (10-ring) [010] 3.5×4.8 Å (8-ring)	2-D intersecting pore system. Both pores are puckered; not very spacious.
TON (ZSM-22) Orthorhombic 13.8×17.4×5.0	[001] 4.4×5.5 Å (10-ring)	1-D puckered pore system.
MFI (ZSM-5) Orthorhombic 20.1×19.9×13.4	[010] 5.3×5.6 Å (10-ring) [100] 5.1×5.5 Å (10-ring)	Intersecting straight [010] and sinusoidal channels [100]. Intersections are quite spacious.
MTT (ZSM-23) Orthorhombic 5.0×21.5×11.1	[001] 4.5×5.2 Å (10-ring)	1-D pore system with puckered pores. Very constricted pore, similar to 8-ring character.
ERI (erionite) Orthorhombic 13.3×13.3×14.8	[001] 3.6×5.1 Å (8-ring)	2-D pore system. Network of large pockets connected by thin 8-ring windows.

transition-state formation, γ will have a value near 1. When severe confinement effects are present, γ will be nearly zero, indicating that the bimolecular mechanism is prohibited.

Quantities γ^{nC6} and γ^{3mC5} were computed for each of the zeolites listed in Table 2, with results summarized in Table 3. The most striking feature of these results is that some small-pore zeolites have very small ($<10^{-6}$) values of γ^{nC6} and γ^{3mC5}. Thus, in MTT and FER, the formation of a bimolecular transition state for either reactant is assumed to be highly unlikely. In TON, the formation of $3mC5_b^{TS}$ is strongly hindered, but the formation of $nC6_b^{TS}$ is possible. This is also the case in MTW where, although the value of γ^{3mC5} is on the same order as MFI, there were highly constrained and unrealistic geometries of $3mC5_b^{TS}$ generated during the calculation. In other words, there was no suitable position in MTW for the transition state to reside. The conclusion is that a purely bimolecular mechanism is not possible in MTT, FER, TON, and MTW, so the evaluation of CI_b is inappropriate for these structures.

In presenting the results of this work, it is most useful to classify the different zeolite structures into groups, based on the predominant selectivity effect seen in each. These selectivity effects can be inferred from the agreement between computed and measured relative CI values. The mechanism for CI_m assumes that cracking is monomolecular and that the observed CI arises from the adsorption selectivity of reactants. The mechanism for CI_b assumes that cracking is bimolecular and that observed CI values are based upon transition-state selectivity. It is not expected that all zeolites

Table 3. Index (γ) for All Zeolites

Zeolite	γ^{nC6}	γ^{3mC5}
FAU	1	1
MOR	1.21434	0.15579
BEA	1.73782	0.08433
MWW	0.66962	0.45583
EUO	0.09298	0.00439
MTW	0.35474	**0.00048**
OFF	0.48875	0.15886
FER	**≈ 0**	**≈ 0**
TON	0.00553	**≈ 0**
MFI	0.14798	0.00096
MTT	**≈ 0**	**≈ 0**
ERI	0.96772	0.15526

Note: Values are normalized by the spacious zeolite FAU. Values near 1 indicate minimal confinement effects on bimolecular transition-state formation. Very small values indicate great confinement barriers to transition-state formation. Values indicated by (**≈ 0**) were less than 10^{-6}. Bimolecular transition-state formation is not possible in these zeolites. We also conclude that the formation of $3mC5_B^{TS}$ is not possible in MTW due to the highly constrained and unrealistic geometries generated during the calculations.

will fall cleanly into one of these two categories. The agreement/disagreement of CI_m and CI_b with experiment can be used, however, to identify the predominant selectivity effect in each zeolite. Five groups of zeolites can be identified, each of which exhibits a different selectivity effect.

Group I. The zeolite pores are so small that the formation of the bimolecular transition state is impossible for either reactant. That is, γ^{3mC5} and γ^{nC6} are essentially zero, and CI_b cannot be computed. The cracking mechanism is consistent with the monomolecular formulation, and the observed selectivity is due to preferential adsorption of the reactants.

Group II. The zeolite pores are large enough to accommodate the bimolecular transition state, but small enough such that there are some confinement effects for the bimolecular transition states. For this group, a bimolecular reaction is predominant and the selectivity of the reaction is based on restricted transition-state selectivity.

Group III. The zeolite pores/cages are so large that there are no confinement or adsorption selectivity effects whatsoever. Selectivity will be due mainly to electronic effects, and the present analysis cannot be used to predict selectivity or shed light on the cracking mechanism.

Group IV. The zeolite pores/cages are large enough to accommodate the bimolecular *n*-hexane transition state, but not the bimolecular 3-methylpentane transition state. That is, $\gamma^{3mC5} \approx 0$, while γ^{nC6} is finite, making the calculation of CI_b impossible. In addition, the pores are not small enough to yield significant adsorption selectivity effects. In this situation, it is possible that *n*-hexane is cracked by both monomolecular and bimolecular mechanisms, while 3-methylpentane is cracked only via the monomolecular mechanism. Diffusional effects can also play a role in determining selectivity. As in the case of Group III, the current analysis cannot be applied to predict the selectivity of Group IV zeolites.

Group V. The zeolite contains cavities that are large enough to accommodate both transition-state and reactant molecules without confinement effects, yet passage between these cavities is restricted. The selectivity of the reaction comes from differences in the diffusivities of the reactants. Since diffusional effects are not captured in the current model, the selectivity in Group V zeolites cannot be predicted.

From the preceding classification, it is clear that the current computational formalism is only effective in probing selectivity for small- and medium-pore zeolites (Groups I and II), where either transition state confinement or preferential adsorption leads to enhanced selectivity of one species over another. The source of selectivity in Groups III–V cannot be predicted directly. The calculations do give information on the siting of reactants and transition states within Groups III–V zeolites, however, which can give insight into likely sources of selectivity.

As discussed previously, it is necessary to select an appropriate reference zeolite so that computed results can be compared directly with experiments. For the monomolecular mechanism, MTT was chosen as the reference zeolite. It is a Group I zeolite, where the calculation of γ clearly indicates that neither bimolecular transition state can form in the constricted pore network. Thus, comparisons will be made between the experimental $\overline{CI}^{MTT}$ and the computed $\overline{CI}_m^{MTT}$. MFI was chosen as the reference zeolite for the bimolecular mechanism. Haag et al. (1982) have demonstrated that the bimolecular mechanism is responsible for the selectivity observed with MFI. The present calculations agree with this conclusion. The formation of both bimolecular transition states is possible in MFI (see Table 3) and transition-state confinement effects lead to the observed selectivity of *n*-hexane over 3-methylpentane. MFI is therefore classified as a Group II zeolite. Thus, bimolecular results will be normalized by MFI and the experimental $\overline{CI}^{MFI}$ will be compared with the computed $\overline{CI}_b^{MFI}$. Experimental and computed reference CI values are listed in Table 4. All experimental data, except for MCM-22, are taken from the Mobil patent by Morrison (1987). The MCM-22 data are taken from a study by Ravishankar and coworkers (1994). A conclusive match between experiment and simulation that indicates classification as Group I or Group II is indicated by the appearance of the numerical values in bold faced type. What follows are some brief comments and interpretation of the results summarized in Table 4.

FAU (X,Y). FAU has a structure made up of a network of small sodalite cages that form spacious supercages. The sodalite cages are too small for the adsorption of hydrocarbons, leaving only the supercages. Results in Table 3 indicate that both transition states may be readily formed, but the supercages are so large that there is no discernible selectivity from confinement effects, hence the very small computed $\overline{CI}_b^{MFI}$ of 0.01 vs. 0.05 for the experiment. Similar agreement is seen for $\overline{CI}_m^{MTT}$. The cracking mechanism in FAU can be either monomolecular or bimolecular; the present analysis is unable to discern which is more likely. FAU is a Group III zeolite.

MOR (mordenite). MOR is a 1-D 12-ring pore system flanked by 8-ring side pockets. The side pockets are too small for the adsorption of the hydrocarbons in this study. Both

Table 4. CI Data from Experiments and Simulations

		Monomolecular CI		Bimolecular CI		
Zeolite	CI^{EXP}	$\overline{CI}^{MTT}$	$\overline{CI}_m^{MTT}$	$\overline{CI}^{MFI}$	$\overline{CI}_b^{MFI}$	Group
FAU	0.4	0.04	0.01	0.05	0.01	(III)
MOR	0.5	0.05	0.02	**0.06**	**0.05**	(II)
BEA	0.6	0.07	0.02	**0.07**	**0.14**	(II)
MWW	1.0†	0.11	0.01	0.12	0.01	(V)
EUO	2.1	0.23	0.02	**0.25**	**0.16**	(II)
MTW	2.3	0.25	0.04	0.28	N/A	(IV)
OFF	3.7	0.41	0.01	0.45	0.02	(V)
FER	4.5	**0.49**	**0.32**	0.54	N/A	(I)
TON	7.3	0.80	0.14	0.88	N/A	(IV)
MFI	8.3	0.91	0.03	**1.0**		(II)
MTT	9.1	**1.0**		1.10	N/A	(I)
ERI	38	4.18	0.01	4.58	0.04	(V)

Note: All experimental data are from Morrison (1987), except MWW. [The experimental CI value of 1.0 for MCM-22 was obtained from Ravishankar et al. (1994); it should be noted that this group obtained a CI value 1.2 for MOR, which is somewhat different than Morrison (1987)]. Monomolecular results are scaled using the zeolite MTT as a reference. Bimolecular results are scaled using the zeolite MFI (ZSM-5) as a reference. N/A for $\overline{CI}_b^{MFI}$ indicates that formation of one or both bimolecular transition states was determined to be forbidden by free-energy calculations. Reasonable agreement between experiment and simulation that identifies Group I or Group II is denoted with **bold faced type**.

transition-state molecules can be formed in MOR. The pore sizes are on the same order as the sizes of the transition-state molecules, leading to restricted transition-state selectivity. The computed $\overline{CI}_b^{\mathrm{MFI}}$ of 0.05 is in good agreement with the 0.06 seen in the experiments. Conversely, the $\overline{CI}_m^{MTT}$ values are a factor of 5 lower than $\overline{CI}^{\mathrm{MTT}}$ (0.01 vs. 0.05). Thus, cracking in MOR appears to proceed via a bimolecular mechanism in which the selectivity is controlled by the bimolecular transition-state formation. MOR is a Group II zeolite.

BEA (beta). BEA is 2-D system of intersecting 12-ring channels. Similar to MOR, the pores and transition-state molecules are of comparable sizes, again leading to restricted transition-state shape selectivity. Agreement between simulation and experiment is reasonable (0.14 vs. 0.07) for $\overline{CI}_b^{\mathrm{MFI}}$, and less so (0.02 vs. 0.07) for $\overline{CI}_m^{\mathrm{MTT}}$. The CI in BEA appears to be governed by bimolecular transition-state selectivity. BEA is a Group II zeolite.

MWW (MCM-22). MWW has a unique pore architecture consisting of two completely independent 2-D pore systems. One of these is a sinusoidal 10-ring channel network, and the other is a network of large supercages connected by 10-ring windows (Leonowicz et al., 1994). Experimentally, MWW has a CI of about 1, indicating that both *n*-hexane and 3-methylpentane are cracked at equal rates. Since branched species crack at higher rates in the absence of confinement and diffusional effects, the structure of MWW appears to either inhibit the cracking of 3-methylpentane or enhance the cracking of *n*-hexane. The calculations do not capture this effect; the reactants and transition states are all easily accommodated in the supercage, leading to computed reference CI values below those measured experimentally. No firm conclusion can be reached regarding the mechanism, but it is possible that diffusional effects governing the access to the supercages are causing the observed selectivity or that the active sites of this zeolite are not in the supercages at all, meaning that the reactions are occurring in the more constricted 10-ring channels. Either one of these factors could account for the observed selectivity. MWW is a Group V zeolite.

EUO (ZSM-50). EUO consists of a 1-D channel system with spacious side pockets. The fact that $\overline{CI}_b^{\mathrm{MFI}}$ agrees well with the experimental $\overline{CI}^{\mathrm{MFI}}$ (0.16 vs. 0.25) and $\overline{CI}_m^{\mathrm{MTT}}$ does not match experiment (0.02 vs. 0.23) suggests that selectivity in EUO results from confinement of the bimolecular transition states in the side pockets. EUO is a Group II zeolite.

MTW (ZSM-12). MTW has a 1-D, strongly puckered, 12-ring pore system. The pores are puckered so strongly that the CI reaction classifies MTW as a 10-ring zeolite. Calculations of γ indicated that the 3-methylpentane bimolecular transition-state does not form, but that the *n*-hexane bimolecular transition-state could form. Thus a purely bimolecular mechanism for both reactants must be ruled out. However, the agreement with experiment for $\overline{CI}_m^{\mathrm{MTT}}$ is poor (0.04 vs. 0.25). It is likely that the selectivity comes about because *both* mechanisms are at work in MTW. *n*-Hexane can be cracked via either mechanism, while 3-methylpentane is cracked by the monomolecular mechanism exclusively. MTW is a Group IV zeolite.

OFF (offretite). OFF comprises parallel stacks of large gmelinite cages and smaller cancrinite cages. The large cages are very spacious with 12-ring windows between them. Passage into the smaller cages from the large cages is through small 8-ring windows. The calculations predict no significant selectivity based on confinement effects for either mechanism. Experimentally, *n*-hexane is found to be preferentially cracked. The lack of selectivity predicted by the calculations arises because both reactants can freely adsorb in the large cages, and both bimolecular transition-states can form there as well. However, it has been reported that the active site in OFF is likely located at the center of the smaller cage (Campana et al., 1997). The experimentally observed selectivity for *n*-hexane cracking is thus likely due to the difference in reactant mobility through 8-ring windows of the small cages. OFF is a Group V zeolite.

FER (ZSM-35). FER is a 2-D intersecting pore system with 8 rings and 10 rings. Evaluation of γ indicated that neither bimolecular transition-state could be formed in the small pores of FER, so the bimolecular mechanism is ruled out. The calculated, $\overline{CI}_m^{\mathrm{MTT}}$ is in good agreement with experiment (0.32 vs. 0.49), indicating that the monomolecular mechanism is proceeding with reactant adsorption controlling selectivity. FER is a Group I zeolite.

TON (ZSM-22). TON is a 1-D puckered system of 10-ring pores. Computed values of γ indicate that the formation of the bimolecular 3-methylpentane transition-state is not possible in TON, but that the bimolecular *n*-hexane transition-state could form. The results for TON can be explained in the same way in which those for MTW were explained. TON is a Group IV zeolite.

MFI (ZSM-5). MFI is 2-D intersecting 10-ring pore system. This zeolite is used as the standard for bimolecular transition-state selectivity. The transition-states are formed in the intersections of the zeolite and fit rather tightly. Calculations of $\overline{CI}_m^{\mathrm{MTT}}$ predict only slight selectivity, in disagreement with experiment (0.03 vs. 0.91). This result helps confirm that cracking in MFI is bimolecular, and that selectivity is based on transition-state formation. MFI is the defining member of Group II.

MTT (ZSM-23). MTT is a 1-D puckered 10-ring system. It is used as the standard for monomolecular reactant adsorption selectivity. Values of γ indicate that formation of both bimolecular transition states are forbidden. Cracking proceeds via a monomolecular mechanism with reactant selectivity. MTT is the defining member of Group I.

ERI (erionite). ERI is a 2-D pore system consisting of large cavities connected by 8-ring windows. ERI has the highest experimental CI of any of the zeolites examined, yet the calculations predict almost no selectivity for either mechanism. ERI illustrates a case where diffusional limitations of the reactants are likely dominant. The superior mobility of *n*-hexane over 3-methylpentane through the 8-ring windows gives rise to the high selectivity. Cracking is governed by reactant selectivity, but the mechanism is not limited to monomolecular. The cavities of ERI are large enough to easily accommodate both the bimolecular transition states. ERI is a member of Group V.

Good agreement between experimental and computed values for $\overline{CI}_m$ and $\overline{CI}_b$ is only to be expected for Group I and Group II zeolites, respectively. Even for zeolites that exhibit similar experimental values of CI, the current work shows that the dominant cracking selectivity effects can be quite different. This is clearly illustrated in Figures 2 and 3. Figure 2

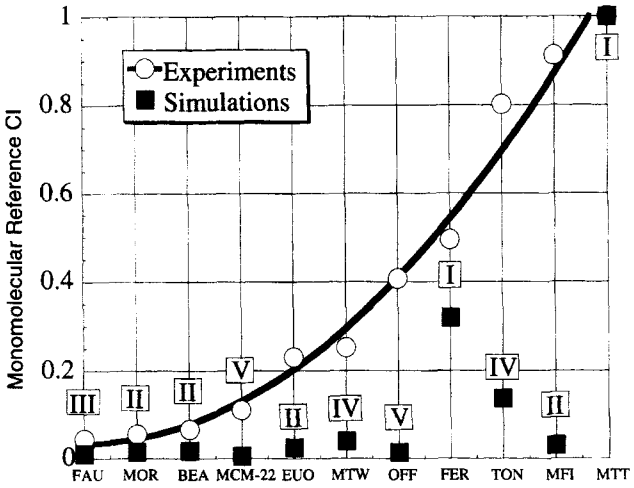

Figure 2. Calculated $\overline{CI}_m^{MTT}$ vs. experimental $\overline{CI}^{MTT}$ values for the monomolecular mechanism.

The reference zeolite is MTT. Group classification is also indicated. Group I zeolites correlate well with experiments, while all others are underpredicted.

compares the computed monomolecular reference CI ($\overline{CI}_m^{MTT}$) vs. the experimental reference CI ($\overline{CI}^{MTT}$). The resulting zeolite group classification is indicated as well. Figure 3 compares computed values of $\overline{CI}_b^{MFI}$ with experimentally measured $\overline{CI}^{MFI}$. Zeolite group classifications are also shown. Notice that there are no Group I or Group IV zeolites on Figure 3 because the calculation of $\overline{CI}_b$ was not appropriate for these groups. As expected, only Group I zeolites show a good match between $\overline{CI}_m^{MTT}$ and $\overline{CI}^{MTT}$, while only Group II zeolites show a match between $\overline{CI}_b^{MFI}$ and $\overline{CI}^{MFI}$.

Even when the computed and measured reference CI values disagree, the result is useful. For instance, in the case of Group V zeolites, transport effects were identified as the

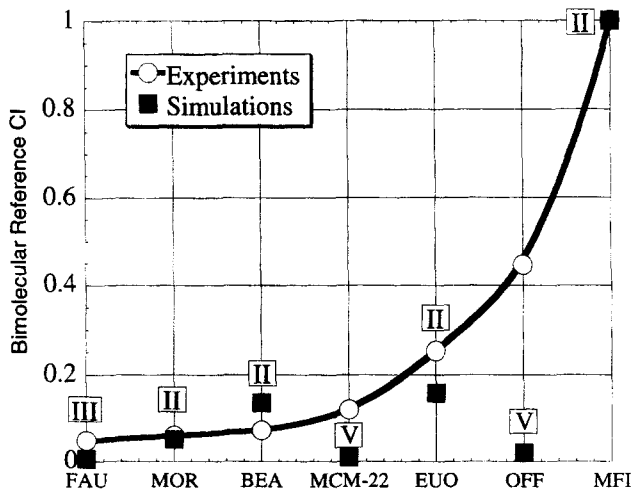

Figure 3. Calculated $\overline{CI}_b^{MFI}$ vs. experimental $\overline{CI}^{MFI}$ values for the bimolecular mechanism.

The reference zeolite is MFI for this case. Group classification is also indicated. Group II zeolites correlate well with experiments, while all others are underpredicted.

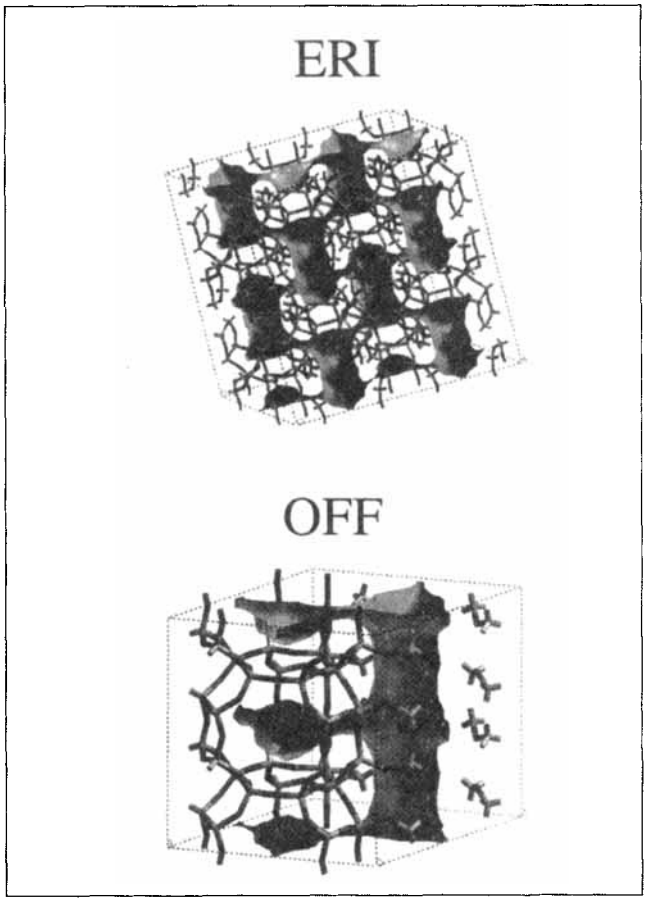

Figure 4. In Group (V) zeolites ERI and OFF, 8-ring bottlenecks in the pores present limitations to reactant diffusion.

Molecules must pass through the 8-rings of ERI to diffuse at all. Molecules must pass through the 8-rings of OFF to reach the active site at the center of the cancrinite cage.

source of selectivity from an analysis of the reactant and transition state conformations inside the cavities. Two such zeolites are ERI and OFF, shown in Figure 4 with the unit-cell pore volumes illuminated by considering a carbon atom probe at an energy of 8 kJ/mol. In both of these cases, formation of the bimolecular transition states is possible, yet diffusional limitations are also important. ERI suffers from diffusional limitations because all molecules must pass through the 8-ring pores in order to pass from one cavity to the next. The situation in OFF is different in that molecules can diffuse freely in the large 12-ring pore, but must pass through the small 8-ring window and into the small cage to reach the active site. The disagreement between the computed $\overline{CI}_b^{MFI}$ and $\overline{CI}_m^{MTT}$ with the corresponding experimental values lends support to these conclusions.

The temperature dependence of the CI in the zeolite MFI has previously been attributed to a change in mechanism from bimolecular at low temperature to monomolecular at high temperature (Haag et al., 1984, 1991). The temperature dependence of $\overline{CI}_b^{MFI}$ for MFI was also investigated and is compared with the experimental observations of Frillette et al. (1981) in Figure 5. The reference temperature for $\overline{CI}_b^{MFI}$ was

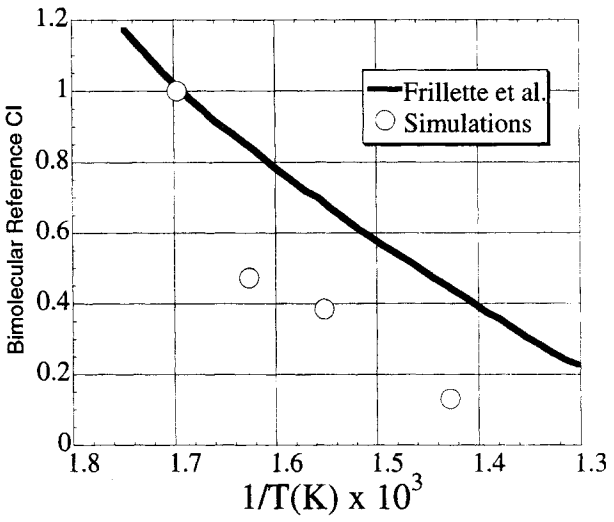

Figure 5. Temperature dependence of $\overline{CI}^{MFI}$ for ZSM-5 as measured by Frillette and coworkers (1981) vs. simulations of $\overline{CI}_b^{MFI}$.

The reference temperature is 589 K. A reduction in the CI with increasing T is seen in both simulations and experiments. A change in mechanism from bimolecular to monomolecular has been used previously to rationalize the reduction of CI with T (Haag and Dessau, 1984; Haag et al., 1991). The reduction is seen in the simulation that assumed a bimolecular mechanism throughout.

589 K. The calculations follow the experimental trend of decreasing CI with increasing temperature without switching to a monomolecular mechanism. In fact, the temperature dependence of the monomolecular mechanism was also investigated by computing $\overline{CI}_m^{MTT}$ as a function of temperature. Interestingly, $\overline{CI}_m^{MTT}$ decreases only about 10% over the entire temperature range. On the other hand, $\overline{CI}_b^{MFI}$ shows a decrease of almost 90%, which is in fairly good agreement with the experiments. Thus, one can conclude that it is not necessary to invoke a change in mechanism to explain the reduction of CI for MFI that occurs with increasing temperature. The present calculations show that the impact of confinement on the bimolecular transition state decreases with increasing temperature, which leads to a reduction in the CI. This is caused by a competition between energetic confinement effects that dominate at lower temperatures and entropic effects that become dominate at high temperature. Of course, the present analysis completely ignores the electronic portion of the rate constant, which would also tend to reduce the CI at high temperatures, given that the activation energy for the monomolecular mechanism is thought to be much higher than the barrier for the bimolecular mechanism. The present work does point out, however, that one must also consider the free energy of adsorption for the activated complexes when computing relative reaction rates. Simple energy minimization procedures or cluster models will not capture these effects.

Conclusions

A method has been developed that can help to gauge the impact that adsorption and restricted transition-state selectivity have on the n-hexane and 3-methylpentane cracking reactions of the "constraint index" test. This method, which is based on a classic molecular mechanics model in a transition-state theory framework, has proven to be predictive for small- to medium-pore zeolites. The cracking selectivity of Group I zeolites, which include MTT and FER, arises from the adsorption selectivity of reactants. The cracking selectivity of Group II zeolites, which include MFI, MOR, BEA, and EUO, arises because of restricted transition-state selectivity associated with the formation of transition-state complexes in the classic bimolecular cracking mechanism. In other zeolites, where adsorption and restricted transition-state selectivity are not the dominant effects, the results of this study can be used to identify the most probable effects leading to observed reaction selectivity. These effects include transport limitations, as well as simultaneous monomolecular and bimolecular cracking mechanisms. It has also been shown that this simulation method can be used to investigate the temperature dependence of reaction selectivity. It was found that reaction selectivity can drastically decrease with increasing temperature (due to entropic effects), while still proceeding by the same mechanism. This is contrary to the traditional reasoning for this effect, which assumed a change in mechanism (Haag et al., 1982, 1991).

Since this study has focused only on adsorption and restricted transition-state selectivity, further progress may be made by examining other effects with additional computational methods. For instance, reactant transport effects could be examined by molecular dynamics or by transition-state transport theory for diffusing species (June et al., 1991). The area of hybrid quantum mechanics/molecular mechanics simulations shows great promise for the investigation of acid catalyzed reactions in zeolites (Sierka and Sauer, 1998). These methods can be used to treat the transition-state complexes more effectively by generating their conformations around the actual active site locations while also providing an avenue for direct evaluation of the electronic contributions to reaction-rate constants. Confinement effects can be captured by the molecular mechanics portion of the technique. A combination of many simulation methods will be necessary to gain a complete understanding of this very complex problem.

Acknowledgments

We acknowledge financial support from the National Science Foundation CAREER program under Grant CTS-9701470, and the U.S. Army Research Office under Grant DAAG55-98-1-0091. Texaco is thanked for providing a fellowship to one of the authors (M.D.M.) through the Center for Catalysis and Reaction Engineering.

Literature Cited

Babitz, S. M., B. A. Williams, J. T. Miller, R. Q. Snurr, W. O. Haag, and H. H. Kung, "Monomolecular Cracking of n-Hexane on Y, MOR, and ZSM-5 Zeolites," *Appl. Catal. A*, **179**, 71 (1999).

Boronat, M., P. Viruela, and A. Corma, "A Theoretical Study of the Mechanism of the Hydride Transfer between Alkanes and Alkenes Catalyzed by an Acidic Zeolite," *J. Phys. Chem.*, **102**, 9863 (1998).

Campana, L., A. Selloni, J. Weber, and A. Goursot, "Cation Siting and Dynamical Properties of Zeolite Offretite from First-Principles Molecular Dynamics," *J. Phys. Chem. B*, **101**, 9932 (1997).

Derouane, E. G., "Zeolites and Solid Solvents," *J. Mol. Catal. A*, **134**, 29 (1998).

Dewar, M. J. S., and W. Theil, "Ground States of Molecules. 38. The MNDO Method. Approximations and Parameters," *J. Amer. Chem. Soc.*, **99**, 4899 (1977).

Frillette, V. J., W. O. Haag, and R. M. Lago, "Catalysis by Crystalline Aluminosilicates: Characterization of Intermediate Pore-Size Zeolites by the 'Constraint Index'," *J. Catal.*, **67**, 218 (1981).

Haag, W. O., and R. M. Dessau, "Duality of Mechanism for Acid-Catalyzed Paraffin Cracking," *Proc. Int. Congr. Catalysis (II)*, Verlag Chemie, Weinham, p. 305 (1984).

Haag, W. O., R. M. Dessau, and R. M. Lago, "Kinetics and Mechanism of Paraffin Cracking with Zeolite Catalysts," *Chemistry of Microporous Crystals: Proceedings of the International Symposium on Chemistry of Microporous Crystals*, Elsevier, Amsterdam, p. 255 (1991).

Haag, W. O., R. M. Lago, and P. B. Weisz, "Transport and Reactivity of Hydrocarbon Molecules in a Shape-Selective Zeolite," *Faraday Discuss. Chem. Soc.*, **72**, 317 (1982).

Hagler, A. T., S. Lifson, and P. Dauber, "Consistent Force Field Studies of Intermolecular Forces in Hydrogen-Bonded Crystals. 2. A Benchmark for the Objective Comparison of Alternative Force Fields," *J. Amer. Chem. Soc.*, **101**, 5122 (1979); *Discover User's Manual*, Molecular Simulations Inc., 9685 Scranton Road, San Diego, CA USA.

Kazansky, V. B., I. N. Senchenya, M. Frash, and R. A. van Santen, "A Quantum-Chemical Study of Adsorbed Nonclassical Carbonium Ions as Active Intermediates in Catalytic Transformations of Paraffins. I. Protolytic Cracking of Ethane on High Silica Zeolites," *Catal. Lett.*, **27**, 345 (1994).

Kazansky, V. B., M. V. Frash, and R. A. van Santen, "Quantum-Chemical Study of the Nonclassical Carbonium Ion-Like Transition States in Isobutane Cracking on Zeolites," *Proc. Int. Congr. Catalysis—40th Anniversary (B)*, Elsevier, Amsterdam, p. 1233 (1996).

Kazansky, V. B., "Adsorbed Carbocations as Transition States in Heterogeneous Acid Catalyzed Transformations of Hydrocarbons," *Catal. Today*, **51**, 419 (1999).

June, R. L., A. T. Bell, and D. N. Theodorou, "Prediction of Low Occupancy Sorption of Alkanes in Silicalite," *J. Phys. Chem.*, **94**, 1508 (1990).

June, R. L., A. T. Bell, and D. N. Theodorou, "Transition-State Studies of Xenon and SF_6 Diffusion in Silicalite," *J. Phys. Chem.*, **95**, 8866 (1991).

Laidler, K. J., *Theories of Chemical Reaction Rates*, McGraw-Hill, New York (1969).

Leonowicz, M. E., J. A. Lawton, S. L. Lawton, and M. K. Rubin, "MCM-22: A Molecular Sieve with Two Independent Multidimensional Channel Systems," *Science*, **264**, 1910 (1994).

Macedonia, M. D., and E. J. Maginn, "A Biased Grand Canonical Monte Carlo Method for Simulating Adsorption Using All-Atom and Branched United-Atom Models," *Mol. Phys.*, **96**, 1375 (1999).

Maesen, Th. L. M., M. Schenk, T. J. H. Vlugt, J. P. de Jonge, and B. Smit, "The Shape Selectivity of Paraffin Hydroconversion on TON-, MTT-, and AEL-Type Sieves," *J. Catal.*, **188**, 403 (1999).

Maginn, E. J., A. T. Bell, and D. N. Theodorou, "Sorption Thermodynamics, Siting, and Conformation of Long *n*-Alkanes in Silicalite as Predicted by Configurational-Bias Monte Carlo Integration," *J. Phys. Chem.*, **99**, 2057 (1995).

Martens, J. A., J. Perez-Pariente, A. Corma, and P. A. Jacobs, "Isomerization and Disproportionation of *m*-Xylene Selectivities Induced by the Void Structure of the Zeolite Framework," *Appl. Catal.*, **45**, 85 (1988).

Martens, J. A., M. Tielen, P. A. Jacobs, and J. Weitkamp, "Estimation of the Void Structure and Pore Dimensions of Molecular Sieve Zeolites Using the Hydroconversion of *n*-Decane," *Zeolites*, **4**, 98 (1984).

Morrison, R. A., "Production of Butanes from Propane," U.S. Patent No. 4,686,316 [Assigned to Mobil Oil Corp (1987)].

Nicholas, J. B., "Density Functional Theory Studies of Zeolite Structure, Acidity, and Reactivity," *Top. Catal.*, **4**, 157 (1997), and references therein.

Pines, H., *The Chemistry of Hydrocarbon Conversion*, Academic Press, New York, p. 83 (1981).

Ravishankar, R., T. Sen, V. Ramaswamy, H. S. Soni, S. Gamapathy, and S. Sivasankar, "Synthesis, Characterization, and Catalytic Properties of Zeolites PSH-3/MCM-22," *Zeolites and Related Microporous Materials: State of the Art 1994*, Elsevier, Amsterdam, p. 331 (1994).

Santilli, D. S., T. V. Harris, and S. I. Zones, "Inverse Shape Selectivity in Molecular Sieves: Observations, Modelling, and Predictions," *Microporous Mater.*, **1**, 329 (1993).

Sauer, J., "Structure and Reactivity of Zeolite Catalysts: Atomistic Modelling Using Ab Initio Techniques," *Zeolites and Related Microporous Materials: State of the Art 1994*, Elsevier, Amsterdam, p. 2039 (1994).

Sierka, M., and J. Sauer, "Application of a Combined Quantum Mechanics—Interatomic Potential Functions Technique for Structure, Properties, and Reactivity of Zeolite Catalysts," *J. Mol. Graph. Model.*, **16**, 274 (1998).

van de Runstraat, A., J. A. Kamp, P. J. Stobbelaar, J. van Grondelle, S. Krijnen, and R. A. van Santen, "Kinetics of Hydro-Isomerization of *n*-Hexane Over Platinum Containing Zeolites," *J. Catal.*, **171**, 77 (1997).

van Santen, R. A., "The Cluster Approach to Molecular Heterogeneous Catalysis," *J. Mol. Catal. A*, **115**, 405 (1997).

Webb, E. B., and G. S. Grest, "Influence of Intracrystalline Diffusion in Shape Selective Catalytic Test Reactions," *Catal. Lett.*, **56**, 95 (1998).

Weitkamp, J., and S. Ernst, "Catalytic Test Reactions for Probing the Pore Width of Large and Super-Large Pore Molecular Sieves," *Catal. Today*, **19**, 107 (1994).

Williams, B. A., S. M. Babitz, J. T. Miller, R. Q. Snurr, and H. H. Kung, "The Roles of Acid Strength and Pore Diffusion in the Enhanced Cracking Activity of Steamed Y Zeolites," *Appl. Catal. A*, **177**, 161 (1999).

Zones, S. I., and T. V. Harris, "The Constraint Index Revisited: Anomalies Based Upon New Zeolite Structure Types," *Mesoporous Microporous Mat.*, **35–36**, 31 (2000).

Manuscript received Jan. 5, 2000, and revision received June 12, 2000.